Vol. 03, No. 02, pp. 74 –80 (2022)
ISSN: 2708-0757

JOURNAL OF APPLIED SCIENCE AND TECHNOLOGY TRENDS

www.jastt.org

Impact of land cover change on land surface temperature over Greater Beirut Area – Lebanon

Ali Khyami

Department of Geography, Faculty of Humanities, Lebanese University, Beirut, Lebanon

ali_khyami@hotmail.com

Abstract

Remote sensing (RS) technology has been used together with geographic information systems (GIS) to determine the LC types, retrieve LST, and analyze their relationships. The term Greater Beirut Area (GBA) is used to refer to the city of Beirut and its suburbs, which witnessed rapid urban growth after the end of the civil war in the last decade of the twentieth century, due to the increase in the number of its inhabitants, and the prosperity and development of sectors such as; industrial, trade, tourism, and construction. These factors led to a wide change in land cover (LC) types and increased land surface temperature (LST). The results showed an increase in built-up areas by 29.1% and agricultural lands by 6%, while bare land, forests, and seawater decreased by 28.5%, 4.9%, and 1.9%, respectively. These changes caused large differences in the LST between built-up areas and other LC types. The highest LST recorded was in built-up areas (33.03°C in 1985, and 34.01°C in 2020), followed by bare lands (32.61 °C in 1985 and 33.49°C in 2020), cropland (31.23°C in 1985 and 32.17°C in 2020), forest (30.08°C in 1985 and 30.47°C in 2020), and water (24.97°C in 1985 and 28.15°C in 2020). Consequently, converting different LC types into built-up areas led to increases in LST and a changed microclimate.

Keywords: *Land surface temperature (LST), Land Cover (LC), Greater Beirut Area (GBA), Geographic Information System (GIS), Remote Sensing (RS).*

Received: June 30th, 2022 / Accepted: October 19th, 2022 / Online: October 25th, 2022

I. INTRODUCTION

One of the major issues facing cities and urban areas is the change of the LC types and the increase in land surface temperature LST (see, e.g., [1] and references therein). LC can be defined as the physical condition of the surface, and it is divided into several categories such as dense vegetation, agricultural land, waterbody, barren land, and built-up areas [2]. According to changing landscapes, climatic conditions, and soil type, these categories may differ from one place to another. Land use illustrates how people use the land. For example, urban areas are divided into residential areas, industrial areas, and recreational areas, while water bodies are divided into pools, rivers, lakes, and sea. LST is defined as the temperature felt when touching any object on the Earth's surface, such as soil, rocks, grass, and asphalt roads. Changes in the LC affect soil quality, evaporation rates, runoff, albedo, and the amount of the transported sediment, as well as the local climate, by modifying surface temperatures [3].

Urbanization is considered one of the most prominent factors that lead to broad changes in the categories of LC. Green spaces, forests, agricultural areas, and unused lands are converted into residential buildings, commercial centers, industrial areas, roads, recreation areas, and other facilities associated with public services, such as train stations, airports, seaports, and government buildings. Synthetic materials such as asphalt and concrete are used in urban construction, which are impermeable materials that absorb and store solar radiation.

After the end of the civil war in 1990, GBA witnessed rapid and unplanned urban growth in the absence of planning, regulations, and legislation regulating land use. Green spaces of various kinds were eliminated and replaced by buildings and roads, which led to pressure on the quality of the environment and possible modification of the surface temperature (Stone, 2001). Increasing LST in urban areas leads to the necessity of cooling the buildings, which is very costly economically, especially in the summer months, and in an area suffering from

doi: 10.38094/jastt302174

the irregular electric supply. Therefore, studying urban growth in GBA and assessing its negative effects on the local climate is considered an urgent matter that must be highlighted. Over the past decades, remote techniques have been used together with GIS to map the LC, retrieve LST, and give satisfactory results. Remote sensing images are characterized by their spectral, spatial, radiometric, and temporal resolutions [4]. Geographic information systems (GIS) provide a flexible environment for entering, displaying, and analyzing digital data and for showing the results in the form of tables, graphs, and maps [1, 3, 5-7]. This research aims to map the LC types, retrieve LST, and analyze the relationship between them, from 1985 to 2020, over GBA.

II. Study Area

GBA represents the urban agglomeration that includes Beirut (the capital of Lebanon, the governorate center) and the adjacent municipalities of the Mount Lebanon Governorate. It is not considered an independent administrative unit, and it extends into the south, east, and north of Beirut. On the west side, there is the Mediterranean Sea as a natural border. GBA is located between 35° 27′ – 35° 39′ E and 33° 42′ – 33° 58′ N (Fig. 1), at the midpoint of Lebanon's Mediterranean coast, with an area of 250 km2, equivalent to 2.3% of Lebanese territory. No recent population census was conducted because of the sectarian system controlling the country. The latest population statistics for the region were conducted in 2007, and the population was estimated more than 2.2 million people.

GBA is affected by the semi-arid Mediterranean climate. Moderate temperatures and rainfall characterize autumn and spring, winter is rainy and cold, and summer is humid and hot. The average temperature is 22 °C, and the annual average rainfall is about 825 mm. During the civil war (1975-1990), the city's destruction has led to intense urbanization of the north and south coast. In 1963, the urbanized area of GBA formed a region of 68 km^2. In 1987, this area had reached 80 km^2 and expanding to 143 km^2 in 2005 [8].

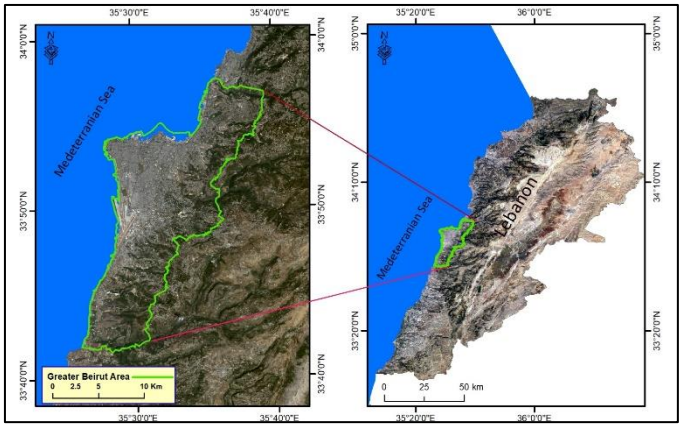

Fig. 1. Map of Greater Beirut Area

III. Materials and Methods

Landsat 5 Thematic Mapper (TM) image for 1985, and Landsat 8 OLITIRS image for 2020 acquired in August, were used to map LC types and show their impacts on LST over GBA. The satellite images were selected according to the criteria adopted by Sun, et al. [1], who suggested the percentage of clouds should be less than 10%. All images used were nearly cloudless. The images were in UTM projection (WGS 84 datum, zone 36 N) and were downloaded from the US Geological Survey (earthexplorer.usgs.gov). Thermal bands were utilized to retrieve LST from Landsat images (band 6 in TM and band 10, 11 in Landsat 8) using the raster calculator tool from ArcGIS software. The three visible bands (blue, green, and red), were combined to obtain true-Color Image. Red and Near Near-Infrared bands were used to extract the normalized difference vegetation index (NDVI). Fig. 2 shows the methodology adopted in the present study, and Table I shows the properties of the Landsat images.

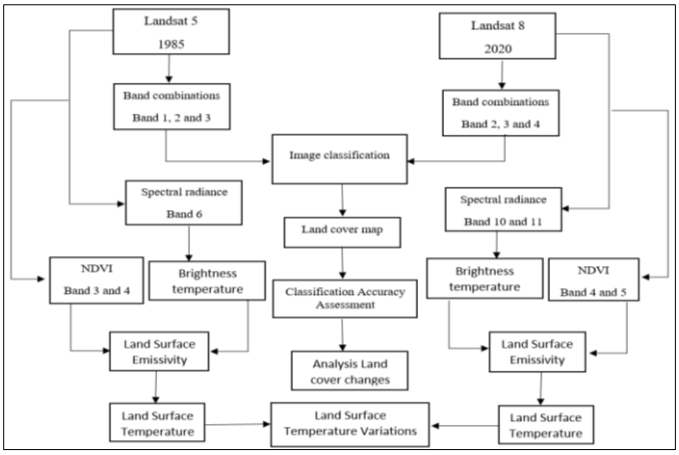

Fig. 2. Flowchart of the Methodology adopted in this study.

TABLE I. The properties of Landsat 5 TM and Landsat 8 images

Satellite	Bands	Wavelength (µm)	Resolution (m)
Landsat 5 TM	Band 1 - Blue	0.45-0.52	30
	Band 2 - Green	0.52-0.60	30
	Band 3 - Red	0.63-0.69	30
	Band 4 - Near Infrared (NIR)	0.76-0.90	30
	Band 5 - Shortwave Infrared (SWIR) 1	1.55-1.75	30
	Band 6 - Thermal	10.40-12.50	120×(30)
	Band 7 - Shortwave Infrared (SWIR) 2	2.08-2.35	30
Landsat 8	Band 1 - Ultra Blue (coastal/aerosol)	0.435 - 0.451	30
	Band 2 - Blue	0.452 - 0.512	30
	Band 3 - Green	0.533 - 0.590	30
	Band 4 - Red	0.636 - 0.673	30
	Band 5 - Near Infrared (NIR)	0.851 - 0.879	30
	Band 6 - Shortwave Infrared (SWIR) 1	1.566 - 1.651	30
	Band 7 - Shortwave Infrared (SWIR) 2	2.107 - 2.294	30
	Band 8 - Panchromatic	0.503 - 0.676	15

Band 9 - Cirrus	1.363 - 1.384	30
Band 10 - Thermal Infrared (TIRS) 1	10.60 - 11.19	100 × (30)
Band 11 - Thermal Infrared (TIRS) 2	11.50 - 12.51	100 × (30)

A. Retrieval of LST from Landsat 5 TM and Landsat 8 OLI

In order to retrieve LST in both Landsat 5 and Landsat 8, four steps have been adopted. The first step varies between the two satellite images. The remaining three steps are the same in Landsat 5 and Landsat 8. Landsat series provide metadata files of the bands, which can be used for retrieval of the LST as illustrated in [9].

a) Conversion of digital number (DN) to Spectral radiance (Lλ): The thermal infrared bands (band 6) of Landsat 5 (bands 10, 11) of Landsat 8 were used to convert digital numbers (DN) values to Spectral radiance. The following equation was used for Landsat 5 [10]:

$$L\lambda = \left(\frac{LMAX - LMIN}{QCALMAX - QCALMIN}\right).(QCAL - QCALMIN) + LMIN \quad (1)$$

Where Lλ is the spectral radiance at the sensor (W M - 2 sr -1 µm-1) Qcal= a digital number of each pixel, Qcalmax= 255, Qcalmin= 0, LMAX is the spectral radiance scaled to Qcalmax (W M - 2 sr -1 µm-1), and LMIN is the spectral radiance scaled to Qcalmin (W M - 2 sr -1 µm-1). While for Landsat 8, the following equation was used (Landsat Project Science Office, 2002):

$$L\lambda = ML.Qcal + AL \quad (2)$$

Where Lλ is the spectral radiance at the sensor (W M - 2 sr -1 µm-1), ML is the Band specific multiplicative rescaling factor (band 10, 11), Qcal is the DN of a given pixel (band 10, 11), and AL is the Band specific additive rescaling factor.

b) Conversion of spectral radiance (Lλ) to at- satellite brightness temperature (TB): The brightness temperature (TB) is the microwave radiation radiance traveling upward from the top of the Earth's atmosphere [5]. Spectral radiance was converted to brightness temperature (TB) by assuming the Earth's surface is a black body [11]. TB for both Landsat- 5 and Landsat- 8 were calculated by using the following equation [10]:

$$TB = \left(\frac{K2}{ln\left(\frac{k1}{L\lambda}\right)} + 1\right) \quad (3)$$

Where TB = Satellite brightness temperature (Kelvin), Lλ = spectral radiance, K1, and K2 are calibration constants for both Landsat 5 (band 6), and Landsat 8 (band 10, 11) (see Table II).

*c) Estimate Land Surface Emissivity:*Land surface emissivity (ε) is the ratio of energy emitted from natural material to that from ideal blackbody at the same temperature [4]. It is desired in land surface models for better simulations of surface energy budgets from which LST is retrieved [12]. Land surface emissivity was calculated as suggested in [13].

$$LSE = 0.986 + Pv \times 0.004 \quad (4)$$

Land surface emissivity $(\varepsilon) = 0.986 + Pv \times 0.004$. Where ε is the Land surface emissivity (LSE), 0.986 and 0.004 are constant emissivity for soil and vegetation cover respectively, Pv is the vegetation proportion obtained according to Carlson and Ripley [12].

$$Pv = \left(\frac{NDVI - NDVI_{min}}{NDVI_{max} - NDVI_{min}}\right)^2 \quad (5)$$

where

NDVI min – NDVI reclassified for soil

NDVI max – NDVI reclassified for vegetation

$$NDVI = \left(\frac{NIR - R}{NIR + R}\right) \quad (6)$$

Where R is the red band, and NIR is the Near Infrared band.

*d) Retrieval of the Land Surface Temperature:*The final step of retrieving the LST, or the emissivity corrected LST, was obtained using the following equation [14].

$$LST = \frac{TB}{\left[1 + \left(\lambda \times \frac{TB}{\rho}\right) \times Ln\varepsilon\right]} \quad (7)$$

Where LST = Land surface temperature in Kelvin, TB = satellite brightness temperature, λ = wavelength of emitted radiance (11.5 µm), ε = land surface emissivity, ρ = h * c/σ (1.438 * 10 -2 mK, (h = Planck's constant = 6.626*10-34 Js, c = light speed =2.998 *108 ms-1, and σ = Boltzmann constant =1.38 * 10_23 J/K^{-1}), finally land surface temperature was retrieved in Kelvin, and converted to Celsius by subtracting 273.15.

TABLE II. CALIBRATION CONSTANT FOR THERMAL BAND

Sensor	K1	K2
Landsat 5 (band 6)	607.76	1260.56
Landsat 8 (band 10)	774.88	1321.08
Landsat 8 (band 11)	480.88	1201.14

B. Image classification

The main purpose of Image classification is to automatically separate similar pixels and place them in different classes that represent the LC types. Two kinds of image classification are widely used, supervised and unsupervised classification [15]. Unsupervised classification is used within the absence of data, high-resolution satellite images, or prior knowledge of the study area. Thus, the image is assessed by software consistent with the number of categories specified by the user. Supervised classification is used when data or satellite images or prior knowledge of the study area is available, and thus, the classification of an image is based on the training areas specified by the user for the software. Supervised classification is one of the most important methods used for quantitative analysis of satellite images. The most common classification algorithms used in supervised classification are Minimum-Distance to the Mean Classifier, Parallelepiped Classifier, and Maximum Likelihood classification [15, 16]. The Maximum Likelihood is derived from the Bayes' theorem and was selected for mapping LC types in this study. It develops the probability function based on inputs from a data set collected from training sites. The

method then considers each pixel in an image, comparing it with known pixels (training sites) and assigning unknown pixels to a LC type based on similarity and highest probability of belonging to an already known type [17, 18].

Based on the visual interpretation of the Landsat image, and the prior knowledge of the study area, five types of LC were identified, forest (dense trees, sparse trees), cropland (Vegetables, grassland), bare land (bare soil, rock), built-up areas (building, industrial areas, roads) and water (only seawater). Each type has different spectral radiation (Fig. 3). Twenty-five training sites as a polygon were signed for all LC types, with an average of five for each category. Then, training samples were entered into the GIS software, and the supervised classification was carried out based on the Maximum Likelihood classification.

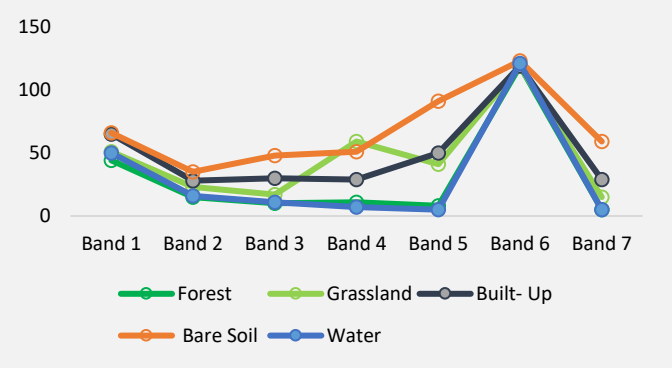

Fig. 3. Spectral reflectance of five land cover types in different bands.

a) Classification Accuracy Assessment: The accuracy assessment is the procedure used to determine the reliability of the classified image. The most commonly used method for evaluating classification accuracy is to create a set of randomly classified points and compare them with the classified images in the error matrix . The error matrix is a multidimensional table that allows visualization of the performance of an algorithm used in image classification. The columns (x-axis) in the table represent the ground truth data, and the rows (y-axis) represent the results of the classified images (or vice versa) (Congalton, 1991). Ground truth data can be derived from interpreting high-resolution images, current the classified images, or from GIS data layers. A total of 150 reference points as samples were randomly distributed over the classified image to check the classification accuracy.

The accuracy assessment measures generated from the error matrix are Producer's accuracy, User's accuracy, Overall accuracy, and Kappa statistic [3, 19, 20].

Producer's accuracy indicates the samples that belong to one type are included in other types. It is also a measure of omission error. The percentage of Producer's accuracy was calculated using the following equation:

$$\text{Producer's accuracy} = \frac{\text{number of correct } \textit{samples} \text{ in a type}}{\textit{sum of samples in the row}} \times 100 \quad (8)$$

User's accuracy indicates the samples that do not belong to one type are included in the same type. It is also a measure of commission error. The percentage of User's accuracy was calculated using the following equation:

$$\text{User's accuracy} = \frac{\text{number of correct } \textit{samples} \text{ in a type}}{\textit{sum of samples in the colum}} \times 100 \quad (9)$$

Overall accuracy indicates the proportion of correctly classified samples on the total number of samples on the map. The percentage of overall accuracy was calculated using the following equation:

$$\text{Overall accuracy} = \frac{\text{Total number of correct samples}}{\textit{Total number of samples.}} \times 100 \quad (10)$$

Kappa coefficient is generally used to assess the accuracy of image classifications. It is mainly based on the difference between how much agreement is presented compared to how much agreement would be expected to be present by chance alone [19]. Kappa coefficient was calculated using the following equation:

$$K = \frac{N \sum_{i=1}^{r} Xii - \sum_{i=1}^{r} (XioXoi)}{N^2 - \sum_{i=1}^{r} (XioXoi)} \quad (11)$$

Where

r = number of rows in the matrix

xii = total number of correct samples in a class

Xio = total of row i

Xoi = total of column i

N = total number of samples in the error matrix

The values of the Kappa coefficient range from -1 to 1. A value of 1 indicates a full match, values less than 0.4 as non to fair match, from 0.4 to 0.55 as moderate, from 0.55 to 0.7 as strong match, from 0.7 to 0.85 as a very strong match, and more than 0.85 as an excellent match in the classified images [21].

IV. Reults and Discussion

A. Analysis Land cover changes

The present study used supervised classification based on the Maximum Likelihood method to produce LC maps from Landsat images. Based on visual interpretation of the image and prior knowledge of the study area, five types of LC were identified: forest, cropland, bare land, built-up areas, and water. Fig. 4 shows the maps after the classification of LC over types over GBA for the years 1985 and 2020.

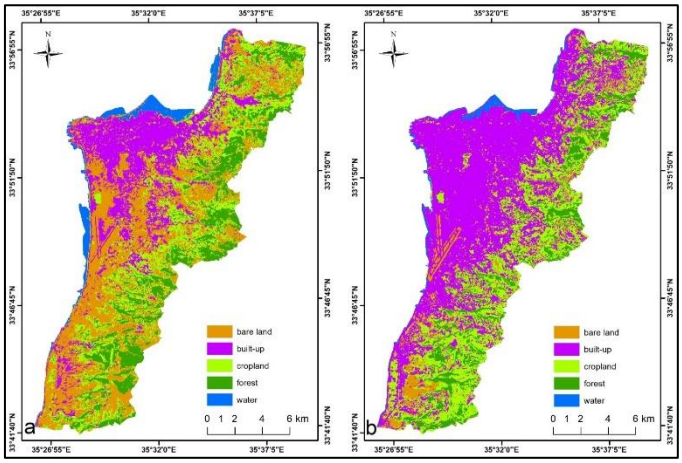

Fig. 4. Land Cover maps of GBA using maximum likelihood classification: (a) 24 August 1985, (b) 24 August 2020.

The produced maps were evaluated for accuracy based on 150 reference points distributed randomly over the LC types for each map 1985 and 2020. Tables III and IV represent the error matrix of the classified image for the year 1985 and 2020. The overall accuracy for the LC maps of 1985 and 2020 was 87% and 89%. The Kappa coefficients were 0.83 and 0.85, respectively. In terms of the user's accuracy the highest percentage recorded was 100% for water (1985 and 2020), and the lowest percentage recorded was 83.33% and 85% for cropland (1985 and 2020). The highest percentage recorded in producer's accuracy was 94.12% in bare lands (1985), and 93.65% in built-up areas (2020), and the lowest percentage was 81.82% in built-up areas (1985), and 83.33 in water (2020). This means that the classification was done with high accuracy, and the method used is appropriate to determine the changes that occur in LC over the years.

TABLE III. ERROR MATRIX FOR THE LAND COVER MAP OF 1985

	Reference data						
Classified data	***Bare lands***	***Built-up***	***Water***	***Forest***	***Cropland***	***Total***	***Users Accuracy (%)***
Bare lands	48	5	0	0	2	55	87.27
Built-up	3	27	0	0	0	30	90
Water	0	0	10	0	0	10	100
Forest	0	1	0	21	3	25	84
Cropland	0	0	2	3	25	30	83.33
Total	51	33	12	24	30	150	
Producers Accuracy (%)	94.12	81.82	83.33	87.5	83.33		
Overall Accuracy (%)							87
Kappa coefficient							0.83

TABLE IV. ERROR MATRIX FOR THE LAND COVER MAP OF 2020

	Reference data						
Classified data	***Bare lands***	***Built-up***	***Water***	***Forest***	***Cropland***	***Total***	***Users Accuracy (%)***
Bare lands	18	2	0	0	0	20	90
Built-up	2	59	1	0	3	65	90.77
Water	0	0	10	0	0	10	100
Forest	0	0	0	13	2	15	86.67
Cropland	1	2	1	2	34	40	85
Total	21	63	12	15	39	150	
Producers Accuracy (%)	85.71	93.6	83.3	86.6	87.1		
Overall Accuracy (%)							89
Kappa coefficient							0.85

The overlay of LC maps for 1985 and 2020 shows considerable changes in the area for each type. The total area of the GBA is about 250 km^2. Table V shows the area and percentage for each type of LC from 1985 to 2020, and Table VI represents the changes that occurred during this period. From these tables, it can be noticed clearly that the built-up areas (building, industrial area, and streets) have the most significant changes, which increased by 29.1% (from 54.20 to 127.05 km^2), this increase was in areas of bare lands, croplands, and water (sea). In contrast, bare lands in the same period decreased by 28.5% (from 91.16 to 20.02 km^2). Meanwhile, the cropland increased by 6% (from 56.62 to 71.50 km^2). However, forest decreased by 4.9% and water by 1.9%.

TABLE V. AREA AND PERCENTAGE FOR LAND COVER IN 1985 AND 2020

	1985		2020	
class	***Area (km^2)***	***Percentage***	***Area (km^2)***	***Percentage***
Bare lands	91.16	36.5	20.02	8
Built-up	54.2	21.7	127.05	50.8
water	8.91	3.6	4.7	1.9
forest	39.1	15.6	26.73	10.7
Cropland	56.62	22.6	71.5	28.6

Based on the previous results (in Tables V and VI), it is clear that built-up areas witnessed the greatest growth and expansion, at the expense of bare land, cropland and forest areas. Southeast of the capital Beirut, where the southern suburb is located, the rate of urbanization has increased dramatically, especially in the areas of Bourj el Barajneh, Haret Hreik, and Chiyah. As for the south of the capital and on the Mediterranean coast, built-up areas swept the agricultural lands in the area of Choueifat, Al-Ozaie, and Khaldeh. The main issue that caused rapid and uncontrolled urbanization in GBA is the absence of legislation regulating land use and the concentration of commercial and

industrial activity in the capital Beirut, which increased the demand on land for urban use. This development required the expansion of public utilities such as roads, airport and port, where the sea areas in Ouzai and Ras Beirut were filled to build the western runway of Beirut airport, and the construction of a new basin in the Beirut port.

TABLE VI. DIFFERENCE BETWEEN AREAS AND PERCENTAGE FOR LAND COVER TYPES FROM 1985 AND 2020

class	Area change from 1985 to 2020 (km^2)	Percentage (%)
Bare lands	-71.1	-28.5
Built-up	72.9	29.1
water	-4.2	-1.7
forest	-12.4	-4.9
Cropland	14.9	6

B. Temperature Variations for different land cover types

LST maps were prepared based on the Thermal Infrared bands of Landsat images using the raster calculator tool from ArcGIS software. LST was retrieved by the conversion of the digital number into the spectral radiance, then the spectral radiance is converted to a satellite brightness temperature. After this process, emissivity was calculated as suggested in Sobrino et al., 2004, and the LST obtained in Kelvin and transformed into degrees Celsius by subtracting 273.15 from the result.

For both images the lowest LST observed was in the water (24.97°C in 1985, and 28.15°C in 2020). Forest recorded (30.08°C in 1985, and 30.47°C in 2020), cropland (31.23°C in 1985, and 32.17°C in 2020), bare lands (32.61. °C in 1985, and 33.49°C in 2020), and built-up (33.03°C in 1985, and 34.01°C in 2020).

The Forest shows the lowest LST after water because it contains a variety of dense trees, which can reduce the amount of heat stored in the soil and surface structures through evapotranspiration, leading to lower temperatures compared to other types of LC. The standard deviations of the LST values are small for water and forest in both years, this is due to the homogeneity of the water (seawater) and forest (pine and oak trees) existing in the study area. Cropland showed middle standard deviation, while built-up area showed the highest level of standard deviation in both years due to the heterogeneity of the material used in building, roads, and general amenities.

The spatial distribution of LST in 1985 and 2020 images is illustrated in Fig. 5. The surface temperature of the 1985 image ranged from 24.9 to 39.9 (average 31.8˚C), and for 2020 ranged from 28. 1 to 41.5 (average 33.02 °C). It is clear that for both images 1985 and 2020, built-up areas followed by bare lands exhibit the highest LST in capital Beirut and the surrounding suburbs, while the lowest LST was recorded in the west (Mediterranean Sea) and in the east (forest). This indicates replacing the LC types (water, forests, cropland, and bare lands) by built-up areas, which by their nature store heat, increases LST and contributes to modifying local climate. The average value of LST and LC types in 1985 and 2020 are illustrated in Table VII.

TABLE VII. AVERAGE VALUES OF LST BY LAND COVER TYPES IN 1985 AND 2020

Class	Average LST 1985	Standard deviation	Average LST 2020	Standard deviation
Built-up	32.61	1.39	34.1	1.57
Bare lands	32.03	1.8	33.49	2.1
Forest	30.08	1.14	30.47	0.86
Cropland	31.23	1.37	32.17	1.22
Water	26.64	0.47	28.71	0.49

The technique of image differentiation (Image 2020 subtracted from Image 1985) was used to detect LST changes that resulted from the changes of LC types. The result has shown that the average LST difference between the areas that were built-up and continued as well, the temperature rose by 1.49°C, and the areas that were transformed from bare lands, cropland, forest, and water into a built-up, LST rose 2.07, 2.87, 4.02, and 7.46 respectively. The area was forest and continued as well. The average temperature rose by 0.39°C, the areas were transformed from bare lands and cropland into the forest due to the plantation campaigns, LST decreased 2.14, 1.56, and 0.76 degrees, respectively. This indicates replacing the LC types (water, forests, and grasslands) with urban areas, which by their nature store heat, increases LST, and contributes to modifying the local climate.

LST map shows that the Ras Beirut region, a built-up surrounded by seawater from the west, north and south, showed lower temperatures than built-up in the surrounding suburbs, indicating a possible effect of sea air contributed to cooling the surface temperature in this region. In some cases and on a limited scale, the LST of bare lands was higher than that of built-up. This was due to low soil depth or rock exposures.

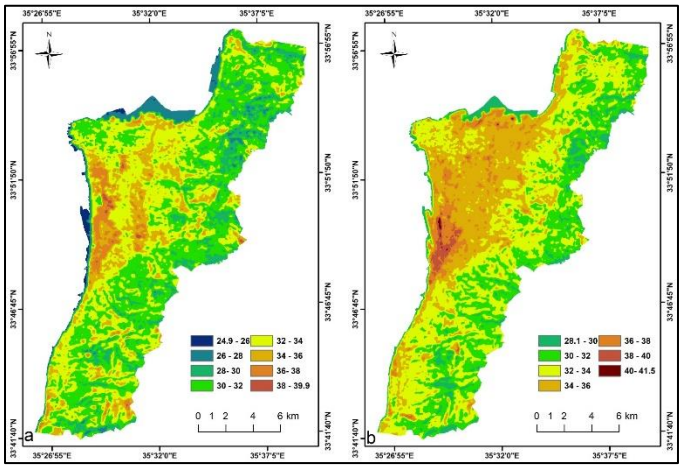

Fig. 5. LST maps of GBA: (a) 24 August 1985, (b) 24 August 2020.

V. CONCLUSIONS

In the present study, an approach of remote sensing (Landsat satellite imagery) and geographic information system were used to evaluate the LC changes and their impacts on LST over GBA. The results showed essential changes between 1985 and 2020, which increased the area of built-up and croplands and

decreased the area of bare lands, forest, and even water (seawater). The most significant change occurred in the capital Beirut and its suburbs, especially in the southern and southeastern, where the area of built-up increases by 29.1 %. The area of bare lands decreased by 28%. These changes led to significant changes in the LST, either positively or negatively. In the case of LC changes to built-up, the temperature rises significantly (from 1.4 to 7.37°C), while in the case of LC changes to a forest, the temperature decreases (from 2.56 to 0.76°C). This study has shown that changing LC types directly affects the local climate and leads to its modification often. This leads to the emergence of urban heat islands at night over cities, where the temperature over urban areas is higher than the temperature in the surrounding rural areas, this is a result of the spread of impermeable surfaces in cities that store heat and do not reflect it, but rather re-emits it to the atmosphere at night.

The limitations of this study were in the difficulty of conducting fieldwork to measure the actual LST and compare it with the LST retrieved from Landsat images. Regarding the classification of the LC types, we could not differentiate between agricultural areas, grassland, and degraded forest, due to the similarity of the spectral reflection of these places, so they have been considered in one category.

The dilemma of finding appropriate solutions to the negative effects of land cover changes lies in the difficulty of implementing them and their high financial cost. In many cases, the problem remains unresolved. For rapidly growing urban, the best recommendation to the decision-makers is to avoid the problem before it occurs. This is through enact the laws and the legislation that regulate land use, distribution of economic activities, public services, and preserving trees and green spaces. For future research, we suggest studying the relationship between LST and air temperature, its impacts on human health, and the ecosystem's members

REFERENCES

[1] Z. Sun, R. Ma, and Y. Wang, "Using Landsat data to determine land use changes in Datong basin, China," *Environmental Geology*, vol. 57, pp. 1825-1837, 2008 2008.

[2] N. R. Khwarahm, "Spatial modeling of land use and land cover change in Sulaimani, Iraq, using multitemporal satellite data," *Environmental Monitoring and Assessment*, vol. 193, no. 3, pp. 1-18, 2021 2021.

[3] S. Pal and S. Ziaul, "Detection of land use and land cover change and land surface temperature in English Bazar urban center," *The Egyptian Journal of Remote Sensing and Space Sciences*, vol. 20, pp. 125-145, 2017 2017.

[4] V. Vijayaraj, N. Younan, and C. O'Hara, "Concepts of image fusion in remote sensing applications," presented at the International Symposium on Geoscience and Remote Sensing, 2006, 2006.

[5] A. Rajeshwari and D. Mani, "Estimation of land surface temperature of dindigul district using Landsat 8 data," *International journal of research in engineering and technology*, vol. 3, no. 5, pp. 122-126, 2014 2014.

[6] S. Gorgani, M. Panahi, and F. Rezaie, "The Relationship between NDVI and LST in the urban area of Mashhad, Iran," presented at the International Conference on Civil Engineering Architecture & Urban Sustainable Development, 2013, 2013.

[7] Y. T. Mustafa, R. T. Ali, and R. M. Saleh, "Monitoring and evaluating land cover change in the Duhok city, Kurdistan region-Iraq, by using remote sensing and GIS," *International Journal of Engineering Inventions*, vol. 1, no. 11, pp. 28-33, 2012.

[8] F. Faour and M. Mhawej, "Mapping Urban Transitions in the Greater Beirut Area Using Different Space Platforms," *Land*, vol. 2073, no. 445X, pp. 941-956, 2014 2014.

[9] R. T. Mzuri, A. A. Omar, and Y. T. Mustafa, "Spatiotemporal Analysis of Land Surface Temperature and Vegetation Changes in Duhok District, Kurdistan Region, Iraq," *The Iraqi Geological Journal*, pp. 68-81, 2022.

[10] G. Chander and B. Markham, "Revised Landsat-5 TM radiometric calibration procedures and postcalibration dynamic ranges," *IEEE Transactions on Geoscience and* Remote *Sensing*, vol. 41, no. 11, pp. 2674-2677, 2003 2003.

[11] O. Orhan and M. Yakar, "Investigating Land Surface Temperature Changes Using Landsat Data in Konya, Turkey," *Remote Sensing and Spatial Information* Sciences, vol. XLI, no. B8, pp. 285-289, 2016 2016.

[12] T. Carlson and D. Ripley, "On the relation between NDVI, fractional vegetation cover, and leaf area index," *Remote Sensing of Environment*, vol. 62, no. 3, pp. 241-252, 1997 1997.

[13] A. Sobrino, C. Jiménez-Muñoz, and L. Paolini, "Land surface temperature retrieval from Landsat TM 5," *Remote Sensing of Environment*, vol. 90, no. 4, pp. 434-440, 2004 2004.

[14] Q. Weng, "A remote sensing–GIS evaluation of urban expansion and its impact on surface temperature in the Zhujiang Delta, China," *International Journal of Remote Sensing*, vol. 22, no. 10, pp. 1999-2014, 2001 2001.

[15] L. Thomas, R. Kiefer, and J. Chipman, *Remote Sensing and Image Interpretation*, 7th ed. Wiley, 2015.

[16] Y. T. Mustafa, "Multi-temporal satellite data for land use/cover (LULC) change detection in Zakho, Kurdistan Region-Iraq," *Environmental Remote Sensing and GIS in Iraq*, pp. 161-180, 2020.

[17] R. J. Jensen, *Introductory Digital Image Processing*, 3rd ed. New York: Prentice Hall, 2005.

[18] A. Kuzucu and F. Balcik, "Testing the potential of vegetation indices for land use/cover classification using high resolution data," *Remote Sensing and Spatial Information Sciences*, vol. IV-4, no. W4, pp. 279-283, 2017 2017.

[19] K. Thakkar, V. Desai, A. Patel, and M. Potdar, "Impact assessment of watershed management programs on land use/ land cover dynamics using remote sensing and GIS," *Remote Sensing Applications: Society and Environment*, vol. 5, pp. 1-15, 2017 2017.

[20] Y. Mustafa, "Spatiotemporal analysis of vegetation cover in Kurdistan region-Iraq using MODIS image data," *Journal of Applied Science and Technology Trends*, vol. 1, no. 1, pp. 01-07, 2020.

[21] R. Monserud and R. Leemans, "Comparing global vegetation maps with the Kappa statistic," *Ecological Modelling*, vol. 62, no. 4, pp. 275-293, 1992 1992.